POLARIMETRIC SCATTERING MODEL FOR METHANE BUBBLES TRAPPED IN THE ICE OF SUB-ARCTIC LAKES

Noora Al-Kahachi, Kostas Papathanassiou

Microwave and Radar Institute
German Aerospace Center

ABSTRACT

In this work we propose a model for the polarimetric backscattering of shallow sub-arctic lakes, which are frozen usually up to two meters depth during winter. The model takes into account the inhomogeneities in the ice layer introduced mainly by CH_4 bubbles trapped in the lake ice. The model is validated against experimental data acquired by ALOS-PalSAR.

Index Terms— sub-arctic lakes, methane bubbles, ellipsoid, dihedral scattering, polarimetric modeling, coherency matrix

1. INTRODUCTION

Thermokarst lakes are known to emit CH_4 gas. However, the magnitude of these emissions remains uncertain since the principal emission mode (ebullition) is highly variable in space and time. Ebullition represents 50-95% of lake methane emissions and increases the previous estimations of northern wetlands methane fluxes by 10-63%. This methane is currently unaccounted in climate change modeling [1].

The analysis of SAR data acquired by RADARSAT-1 (C-band) and ALOS-PalSAR (L-band) over thermokarst lakes made clear that the backscattering from methane bubbles becomes visible in the SAR image implying that SAR may play a role in evaluating methane ebullition from lakes. In [2] a correlation between the backscattered power measured by RADARSAT-1 with field survey data for percent cover of lake ice with bubbles and for point-source ebullition has been observed. The results describe a better correlation in the early winter acquisitions, and steeper look angles. Similar relations are shown in [3]. However relations based on observations are not sufficient for a quantitative evaluation of CH_4 ebullition, thus an adequate modeling of the polarimetric backscattered signature is required.

Any scattering model for the evaluation of CH_4 bubbles trapped in the ice lake should be able to take into account the variety of possible scenarios, see Fig. 1: While on some lakes water freezes to the lake bed and forms grounded ice, on deeper lakes only floating ice is generated during winter. The change in the dielectric properties of the material under the ice influences the backscattering to the SAR system. When floating ice is formed, the backscattered power increases dramatically (around 10 dB at C-band), mainly due to the contribution of the scattering from the ice inhomogeneity that is reflected back on the ice-water interface [3]. The backscattered power is lower when the water freezes to the bed, since the reflection from the ice water interface is replaced by the one from ice-lakebed.

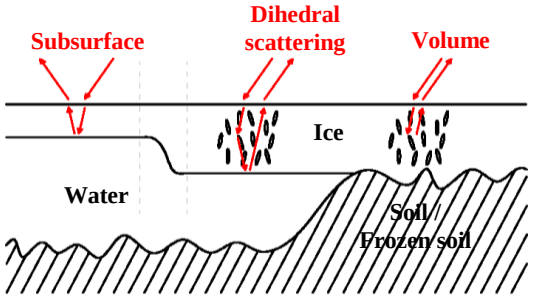

Fig. 1: Scattering scenarios in thermokarst lakes (winter).

2. MODELING OF ICE ABOVE A SURFACE

The proposed model considers three main scattering mechanisms: subsurface scattering from the ice/water or ice/frozen soil interface, volume scattering from the methane bubbles, and dihedral scattering which is generated by scattering from the volume that is reflected by the subsurface. The backscattering from the air-ice surface is neglected, as its power is very low compared to the backscattered power from the ice-water interface and its polarimetric signature is very similar, which will further reduce its influence [4]. The measured coherency matrix $[T_S]$ is then given by:

$$[T_S] = P_{SS}\begin{bmatrix} 1 & T_{12}^{SS} & 0 \\ T_{12}^{*SS} & T_{22}^{SS} & 0 \\ 0 & 0 & T_{33}^{SS} \end{bmatrix} + P_V\begin{bmatrix} 1 & T_{12}^{V} & 0 \\ T_{12}^{*V} & T_{22}^{V} & 0 \\ 0 & 0 & T_{33}^{V} \end{bmatrix} + P_D\begin{bmatrix} 1 & T_{12}^{D} & 0 \\ T_{12}^{*D} & T_{22}^{D} & 0 \\ 0 & 0 & T_{33}^{D} \end{bmatrix} + [T_N] \quad (1$$

The first term corresponds to the back scattering from the subsurface. Information about roughness conditions is not available, but an X-Bragg subsurface is assumed since the X-Bragg model [5] describes well the backscattering from the lakes during summer, where only scattering from the air-water interface is expected. The last term $[T_N]$ stands for the noise coherency matrix.

The second term is the coherency matrix of partially vertically oriented volume of ellipsoids, as will be discussed below. The third term stand for the coherency matrix of the dihedral scattering from first the same volume that contribute with the volume scattering then reflected back by the subsurface. The volume and dihedral backscattering depend strongly on the nature and shape of the bubbles.

More recent observations of lakes with high CH_4 emission describe methane bubbles as tiny bubble tubes (<2 cm diameter) generated at the sediment layer [7]. In general, bubbles rise constantly from

the sediment at the bottom of the lake. The ice is formed layer by layer and the bubbles that rise get trapped in the newly formed layer of ice, generating a columns shape structure.
Accordingly, the particles that form the volume and contribute in the dihedral backscattering are assumed to be vertically oriented ellipsoids as an approximation for the formation described above.

3. MATHEMATICAL FORMULATION OF A VOLUME OF ELLIPSOIDS

An ellipsoid in the Rayleigh scattering region can be modeled using three orthogonal dipoles of different lengths, which span the 3 axes of it [8]. Those three dipoles are also known as polarizabilities (p_1, $p_2 = p_3$). This approach is used to calculate the ellipsoid backscattering, and with the same approach the ellipsoid scattering toward the subsurface can be obtained.

$p_1 = p_2$ $p_1 >> p_2$ $p_1 > p_2$

Fig. 2: Polariszabilities p_1, p_2 and p_3 of a small ellipsoid.

For an incident electromagnetic wave on a dipole, whose polar angle is θ_{inc} and azimuthal angle φ_{inc} = 180°, and a scattering observed at polar angle θ_{obs} and azimuthal angle φ_{obs} = 180°, the power normalized scattering matrix for a single dipole oriented at polar angle θ, and azimuthal angle φ can be derived and is as follows:

$$\left[H\ (\theta,\theta_{inc},\theta_{obs},\varphi)\right]=\begin{bmatrix} S_{hh}^{H} & S_{hv}^{H} \\ S_{vh}^{H} & S_{vv}^{H} \end{bmatrix}$$

$$S_{hh}^{H}=\frac{(1-\cos 2\varphi)(1-\cos 2\theta)}{4}$$

$$S_{hv}^{H}=\sin 2\varphi\cos\theta_{obs}\frac{1-\cos 2\theta}{4}-\sin\varphi\sin\theta_{obs}\frac{\sin 2\theta}{2} \quad (2)$$

$$S_{vh}^{H}=\sin 2\varphi\cos\theta_{inc}\frac{1-\cos 2\theta}{4}-\sin\varphi\sin\theta_{inc}\frac{\sin 2\theta}{2}$$

$$S_{vv}^{H}=\cos\theta_{inc}\cos\theta_{obs}\frac{(1+\cos 2\varphi)(1-\cos 2\theta)}{4}$$

$$-\sin(\theta_{inc}+\theta_{obs})\cos\varphi\frac{\sin 2\theta}{2}+\sin\theta_{inc}\sin\theta_{obs}\frac{1+\cos 2\theta}{2}$$

For an ellipsoid, its polarizabilities are perpendicular to each other and aligned along its principle axes, as shown in Fig. 2. The scattering from the ellipsoid is equivalent to the coherent superposition of the three polarizabilities as in the following:

$$\left[E\ (\theta,\theta_{inc},\theta_{obs},\varphi)\right]=\begin{bmatrix} S_{hh}^{E} & S_{hv}^{E} \\ S_{vh}^{E} & S_{vv}^{E} \end{bmatrix}=p_1\left[H\ (\theta,\theta_{inc},\theta_{obs},\varphi)\right]$$

$$+p_2\left[H\left(\theta+\frac{\pi}{2},\theta_{inc},\theta_{obs},\varphi\right)\right]+p_2\left[H\left(\theta+\frac{\pi}{2},\theta_{inc},\theta_{obs},\varphi+\frac{\pi}{2}\right)\right] \quad (3)$$

The particles usually do not exist alone, but rather in a cloud with a given distribution and different size, shape and orientation. The average of this is seen by the radar, and the total scattering is the incoherent sum of the scattering from the particles.

The volume backscattering can be obtained by setting the incident and observe angles equal to the satellite look angle $\theta_{obs}=\theta_{inc}=\theta_L$. Then the coherency matrix is calculated as follows:

$$\left[T_V\right]=\int_0^{2\pi}\int_0^{\theta_{orientation}}\vec{k}_P(\theta,\varphi)\cdot\vec{k}_P^{*}(\theta,\varphi)\cdot P(\theta)d\theta d\varphi$$

$$where\ \vec{k}_p^{T}=\left[S_{hh}^{E}+S_{vv}^{E}\ S_{hh}^{E}-S_{vv}^{E}\ 2S_{hv}^{E}\right]/\sqrt{2}\ \ and\ \ P(\theta)=\frac{\sin\theta}{4\pi}. \quad (4)$$

The distribution width of the ellipsoid orientation in the polar angle direction is denoted by $\theta_{orientation}$, and $P(\theta)$ is the probability density function of the ellipsoids' orientation angles in the volume. The probability density of the distribution presented in the equation above maintains a uniform distribution of ellipsoids' orientations in a 3D space.
By applying Eigen-decomposition on the coherency matrix [5], the Entropy-Alpha values for the volume scattering at θ_L=25° are shown in Fig. 3(a). In general, the volume of spherically shaped particles (red dots) has lower mean Alpha angle values, and more randomly oriented volumes (blue) larger Entropy.
With a subsurface present, multiple scattering can occur as a sequence of scattering at a particle in the volume followed by the specular reflection at the subsurface interface with Fresnel coefficients ($R_\perp, R_\parallel$). The same particle scatters back another portion of the electromagnetic wave but in a reverse order. The normalized scattering matrix of the backscattering from a dihedral formed by a particle and a subsurface is given by the coherent addition of these two components:

$$\left[S\right]_D=\begin{bmatrix} R_\perp & R_\perp \\ R_\parallel & R_\parallel \end{bmatrix}\cdot\left[E(\theta,\varphi)\right]_{\substack{\theta_{inc}=\theta_L \\ \theta_{obs}=\pi-\theta_L}}+\begin{bmatrix} R_\perp & R_\parallel \\ R_\perp & R_\parallel \end{bmatrix}\cdot\left[E(\theta,\varphi)\right]_{\substack{\theta_{inc}=\pi-\theta_L \\ \theta_{obs}=\theta_L}} \quad (5)$$

The coherency matrix for the dihedral scattering at the ellipsoid volume and subsurface is calculated similar to the coherency matrix of the volume backscattering by implementing Eq. (4) for the dihedral scattering matrix.

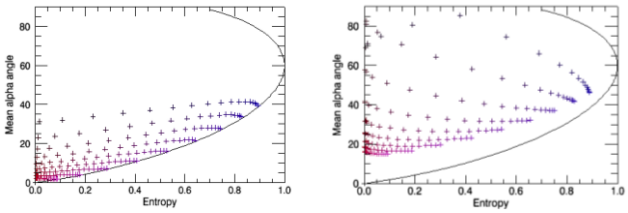

(a) Volume backscattering (b) Dihedral backscattering

Fig. 3: Entropy-Alpha plots at θ_L = 25° and subsurface permittivity of (80+j20). The red colour indicates the shape from dipole (dark red) to spheres (bright red) and blue the orientation from totally (dark blue) to randomly oriented (bright blue) particles.

The resulting Entropy-Alpha distribution of the dihedral scattering of a volume and a subsurface at θ_L=25° is in Fig. 3(b). No large difference in the distribution is observed by changing the subsurface permittivity from water to frozen soil. In general the points show a slightly larger Alpha value compared to the volume backscattering, indicating a larger co-polarization ratio due to the reflection coefficient that increases the horizontal polarization compared to the vertical one. The points cover a wider range of Entropy-Alpha values including the region of the conventional dihedral with Alpha angles above 50°.

Some areas of the Entropy-Alpha distribution of the dihedral mechanism overlap with areas covered by the volume; however the backscattering is different $|HH| > |VV|$.

The dihedral mechanism explains the dependency between the backscattered power and ebullition during early winter and the look angle dependency as mentioned in [2].

4. SCENARIO SIMULATION

The model of Eq. (1) is used to simulate different lakes conditions. The subsurface permittivity is assumed to be 80+j20 for water subsurface and 8+j2 for soil/frozen soil. The ice permittivity is assumed to be 2.5+j0.01. In spite of the pessimistically assumed high value for the imaginary part of the ice permittivity, the influence of the losses within the ice is still negligible for the 2 meters depth. For the subsurface coherency matrix, the X-Bragg model with a distribution width of surface slope angles equal to 30° is used. The subsurface backscattered power coefficient P_{SS} depends mainly on the surface roughness and permittivity. Pre-assumptions of subsurface power contribution are not realistic.

The coherency matrix of the volume and dihedral backscattering depends on the particles shape and orientation, which are expected to vary greatly with space and time. The volume backscattered power coefficient P_V depends on volume density, ice thickness and particle size. Pre-assumptions of volume power contribution are also not realistic. The dihedral backscattered power coefficient P_D depends on the volume scattering in the direction where the scattering is reflected back to the satellite by the subsurface, and the reflection coefficients on the subsurface. For simplicity and since ice thickness is around 1-2 meters, attenuation through the ice layer is neglected. The roughness of the subsurface interface is assumed to be low such that the dihedral backscattered power is approximated by the multiplication of the volume backscattered power by the average of the Fresnel coefficients:

$$P_D = P_V \left(R_\perp + R_\parallel\right)^2 / 4. \quad (6)$$

4.1 Volume and dihedral backscattering

The power contribution of the dihedral compared to the volume contribution is highly dependent on the subsurface permittivity. The high permittivity of the water yield to a higher dihedral backscattering contribution which brings an Entropy-Alpha distribution closer to the maximum Entropy line compared to subsurface frozen soil as can be observed in Fig. 4.

By applying Eq. (6) for the water subsurface, the dihedral contribution represents around 33% of the backscattered power from both volume and dihedral which is the case in Fig. 4(a). For the case of soil subsurface as in Fig. 4(b) the dihedral contribution represent 8% of the backscattered power from volume and dihedral.

In spite of the low contribution from the dihedral component, the entropy values in Fig. 4(b) are effectively increased compared to the volume backscattering in Fig. 3(a). That is because the dihedral backscattering has a higher correlation between $S_{hh} - S_{vv}$ and $S_{hh} + S_{vv}$ channels than the volume backscattering, and opposite in sign for vertically oriented prolate which is the case that is considered here.

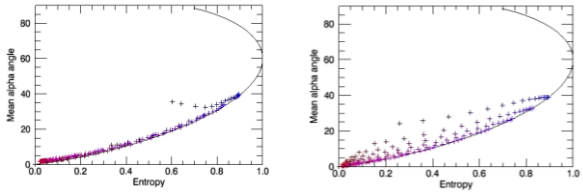

(a) Water subsurface (b) Soil subsurface

Fig. 4: Entropy-Alpha plot for a combination of a volume and dihedral backscattering; at θ_L =25°, for the same particle's shape and orientation distribution used in Fig. 3.

4.2 Subsurface, volume and dihedral backscattering

The forward simulation of the model in Eq. (1) requires an assumption for the volume backscattered contribution as a portion of the total backscattered power. The portion of the dihedral backscattered power contribution is a function of the volume portion and is obtained from Eq. (6). The rest of the power is the subsurface contribution. In this way, every assumption of a volume contribution results in a different Entropy-Alpha distribution.

To simulate the change in the backscattering from floating to grounded ice, the volume backscattered power is assumed to be the same for both cases. The dihedral backscattered power is reduced from the subsurface water to soil by a factor of $(|R_{\perp soil}|+|R_{\parallel soil}|)^2/(|R_{\perp water}|+|R_{\parallel water}|)^2$ which is less than one since the permittivity of water is higher. The subsurface backscattered power is also reduced by a factor of $(R_{h\,soil}+R_{v\,soil})^2/(R_{h\,water}+R_{v\,water})^2$, where (R_h, R_v) are the Bragg scattering coefficients.

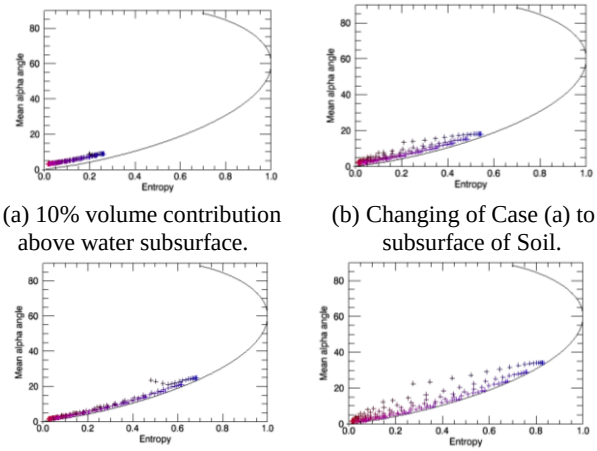

(a) 10% volume contribution above water subsurface.

(b) Changing of Case (a) to a subsurface of Soil.

(c) 40% volume contribution above water subsurface

(d) Changing of Case (c) to a soil subsurface.

Fig. 5: Entropy-Alpha distribution for the model at θ_L =25° for the same particle's shape & orientation distribution shown in Fig. 3.

Fig. 5(a) assumes a low volume contribution to demonstrate a lake that is covered by a thin layer of ice: the volume contribution of 10% results in around 5% dihedral contribution and 85% of the backscattered power corresponds to the subsurface. Fig. 5(b) is a theoretical case of a thin layer of ice above a soil subsurface. The lower subsurface permittivity reduces the backscattered power from the dihedral and subsurface, such that the total backscattered power in Case (b) equals to 1/4 the power for Case (a). The volume

backscattered power contribution is driven to be more dominant and represents 39% of the backscattered power, the dihedral is 3% and the subsurface is 58%. Fig. 5(c) and (d) show a similar investigation with a volume contribution of 40%. The dihedral contribution is 19%, and the subsurface power is 41%. The total backscattered power of Case (d) is 1/2 of the backscattered power from Case (c). The volume contribution is 79%, dihedral 7% and subsurface 14%.

In general, the Entropy and Alpha values increase for grounded ice compared to floating ice, as the volume becomes more dominant. With less dihedral contribution compared to the volume contribution for grounded ice case the distribution is further away from the maximum entropy line

5. RESULTS AND EVALUATION OF ALOS DATA

The forward simulation of the model is compared to fully polarimetric L-Band data obtained by ALOS PalSAR over Churchill region. Winter data contrary to summer over the lakes shows a considerable increase in the horizontal backscattered component compared to the vertical one. The data also shows a zero phase between them. The dihedral scattering from the volume and subsurface fulfills the observed characteristics in the backscattering.

On Churchill site, the acquisition during ice presence (10/5/2009) is considered. The lake samples had been divided into two groups, one with low backscattered power that is assumed to be grounded ice. The other group has high backscattered power and is assumed to be floating ice. The grounded ice group shows an average backscattered power that is around 0.46 of the average power for the samples of the floating ice samples. The Entropy-Alpha histogram for the data is shown in Fig 6(a,b).

According to the analysis presented is section 4.2, a volume power contribution of 35% for floating ice, results in a total backscattered power for grounded ice that has a factor of 0.46 of the power for floating ice. A certain range of volume orientation and particles' shapes is simulated in Fig 6(c,d). The ranges are chosen to produce Entropy and alpha values that cover the same range observed in the histogram of the floating ice. Fig. 6(d) shows the distribution for the exact parameters used to produce Fig. 6(c) but for a soil subsurface instead of water. Both simulation results and data show the same tendency, and vary similarly from floating ice to grounded ice.

Evaluations of data from other sites also follow the expectations obtained by the model, but are not shown here explicitly.

6. CONCLUSION

A model that explains the polarimetric backscattering of shallow subarctic lakes is developed and presented. The model considers the dihedral backscattering from the volume reflected by the subsurface. A mathematical formulation of the coherency matrix for this scattering mechanism is shown and simplified such that the mechanism does not produce additional unknowns to a model that does not consider it. The simulation results show the same tendencies as the observed data for Churchill site.

For further investigation on the model validity, test sites with available on site measurements are required. In addition investigations on improving the model using different or several look angles might improve the evaluation of CH_4 emission and the quantitative determination of the CH_4 content.

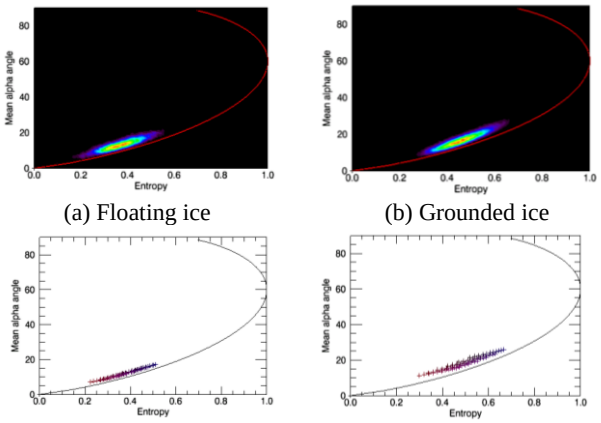

(a) Floating ice (b) Grounded ice

(c) Simulation of floating ice (d) Simulation of grounded

Fig. 6: Entropy-Alpha Histogram for floating and grounded ice over Churchill site compared to simulated Entropy-Alpha distributions.

7. REFERENCES

[1] M.-L. Geai1, K.M. Walter, and G. Grosse1, "Climate Change and Methane Emissions: Pan Arctic Lake Ice Methane Monitoring Network (PALIMMN)", *OSLO science conference*, 2010.

[2] K. M. Walter, M. Engram, C. Duguay, M. Jeffries, and F. S. Chapin, "Potential use of synthetic aperture radar (SAR) for estimating methane ebullition from arctic lakes", *Journal of the American Water Research Association*, 44(2):305-315, 2008.

[3] Claude R. Duguay, Terry J. Pultz, Peter M. Lafleur and D´eborah Drai1, "RADARSAT backscatter characteristics of ice growing on shallow sub-Arctic lakes, Churchill, Manitoba, Canada.", *HYDROLOGICAL PROCESSES* 16, 1631–1644, 2002.

[4] Noora Al-kahachi, Konstantinos P. Papathanassiou, "Polarimetric SAR Investigation for a Two Layer Structure", *EUSAR* 8, 817-820, 2010

[5] Hajnsek, Irena, *Inversion of Surface Parameters Using Polarimetric SAR*, DLR Oberpfaffenhofen, Diss., 2001.

[6] A.R. Phelps, K.M. Peterson, and M.O. Jeffries, "Methane Efflux From High-Latitude Lakes During Spring Ice Melt", *Journal of Geophysical Research* 103(D22):29029-29036, 1998.

[7] K. M. Walter, S. A. Zimov, J. P. Chanton, D. Verbyla, and F. S. Chapin, "Methane bubbling from Siberian thaw lakes as a positive feedback to climate warming", *Nature* 443, 71-75, 7 September 2006.

[8] Van de Hulst, H.C., *Light scattering by Small particles*, Courier Dover Publications, 1957.

[9] Cloude, S. R., *Polarisation: Applications in Remote Sensing*, Oxford University Press, 2010.